Science Advances
AAAS

advances.sciencemag.org/cgi/content/full/7/12/eabf0617/DC1

Supplementary Materials for

Resilient three-dimensional ordered architectures assembled from nanoparticles by DNA

Pawel W. Majewski, Aaron Michelson, Marco A. L. Cordeiro, Cheng Tian, Chunli Ma, Kim Kisslinger, Ye Tian, Wenyan Liu, Eric A. Stach, Kevin G. Yager, Oleg Gang*

*Corresponding author. Email: og2226@columbia.edu

Published 19 March 2021, *Sci. Adv.* **7**, eabf0617 (2021)
DOI: 10.1126/sciadv.abf0617

The PDF file includes:

Other Supplementary Material for this manuscript includes the following:

(available at advances.sciencemag.org/cgi/content/full/7/12/eabf0617/DC1)

Supplementary Materials

Preparation of DNA-gold nanoparticle superlattices

Gold nanoparticle lattices are composed of DNA origami frames and spherical 10 nm or 15 nm gold nanoparticles. DNA origami frame was employed as a linker and scaffold to direct the assembly of gold nanoparticles into lattices. In this report, we used two different face-centered cubic (FCC) lattices and one simple-cubic (SC) lattice to demonstrate the silica coating principle. Here, we provide only the summarized description of the synthesis route leading to the uncoated DNA-gold nanoparticle superlattices; while more details can be found in our previous reports (*26,27*).

The DNA origami frames were designed using *caDNAno* software (http://cadnano.org), and the sequences of the sticky ends binding to the gold nanoparticles were designed using the SEQUIN program (*67*). The M13mp18 DNA genome was purchased from Bayou Biolabs. Staple strands and DNA strands coating gold nanoparticles were purchased from Integrated DNA Technologies, Inc. Gold nanoparticles were purchased from Ted Pella, Inc.

Preparation of DNA-gold nanoparticle conjugates.

Thiolated DNA oligonucleotides were reduced by tris(2-carboxyethyl)phosphine (TCEP) with a molar ratio of DNA to TCEP as 1:100 for 2 hours. Then the oligonucleotides were purified using size exclusion columns (G-25, GE Healthcare) to remove the small molecules. The thiolated oligonucleotides were incubated with aqueous gold nanoparticle solution with a DNA/nanoparticle ratio of 300:1 (10 nm gold nanoparticle) or 800:1 (15 nm gold nanoparticle) for another 2 hours. The solution was then buffered at pH 7.4 in 10 mM phosphate buffer and aged for 2 hours. Salt (2 M NaCl) was gradually added into the solution until the final salt concentration reached 0.3 M. The sample was allowed to age for another 12 hours. Unbound DNA was removed by centrifugation and rinsing with 0.1 M PBS buffer (10 mM phosphate, 0.1 M NaCl).

Self-assembly of DNA tetrahedron frames. The assembly was carried out by mixing 20 nM of M13mp18 DNA genome, 40 nM of anchoring staple strands and 100 nM of other staple strands (final concentrations reported herein) in 1× TAE/Mg^{2+} buffer (40 mM Tris-HCl, pH 8.0, 20 mM acetic acid, 1 mM EDTA, and 12.5 mM magnesium acetate). The mixture was heated at 90 °C for 2.5 minutes, cooled from 90 °C to 70 °C at a rate of 1.5 °C min^{-1}, from 70 °C to 60 °C at a rate of 0.5 °C min^{-1}, from 60 °C to 30 °C at a rate of 0.05 °C min^{-1}, and then cooled from 30 °C to 20 °C at a rate of 0.1 °C min^{-1} in a thermo-cycling machine (Eppendorf).

Self-assembly of FCC lattice composed of DNA tetrahedral frames. As-synthesized DNA tetrahedra were mixed with 14.5 nm spherical gold nanoparticles functionalized with complementary DNA with a molar ratio of 1:1. The sample was heated at 50 °C for 20 minutes and then slowly cooled from 50 °C to 20 °C at a rate of 0.4 °C h^{-1}.

Self-assembly of DNA octahedral and cubic frames. The assembly was carried out by mixing 10 nM of M13mp18 DNA genome and 100 nM of staple strands in 1× TAE/Mg^{2+} buffer (final concentrations). The mixture was heated at 90 °C for 10 minutes, cooled from 80 °C to 60 °C at a rate of 1 °C min^{-1} and then cooled from 60 °C to 20 °C at a rate of 1 °C h^{-1}.

Self-assembly of FCC lattice composed of DNA octahedral frames and SC lattice. 10 nm spherical gold nanoparticles were mixed with corresponding as-synthesized DNA frames with a gold nanoparticle/DNA frame ratio of 2:1. The sample was slowly cooled from 50 °C to 20 °C at a rate of 0.3 °C h^{-1}.

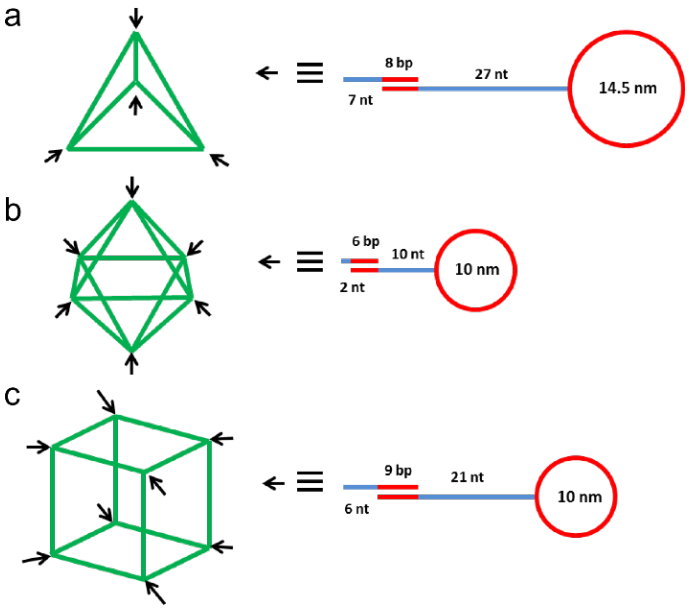

Figure S1. An overview of DNA-AuNPs superlattice building blocks with the locations of gold nanoparticles attachment marked with arrows: (**a**) tetrahedral, (**b**) octahedral (**c**) cubic units.

Morphology of uncoated DNA-gold nanoparticle superlattices

This FCC lattice was assembled by DNA tetrahedron frames and 14.5 nm gold nanoparticles with a molar ratio of 1:1 The DNA tetrahedron was built by six 10-helix bundle edges with a length of 36 nm. Two single-stranded DNA were extended at both ends of each bundle to hybridize complementary DNA strands coated on the nanoparticle. The nanoparticle with a core diameter of 14.5 nm was anchored on each vertex of DNA tetrahedron by six anchoring strands. Each nanoparticle was connected by four DNA tetrahedrons to form an FCC lattice. The assembled lattice was investigated by *in-situ* small-angle x-ray scattering (SAXS). The 2D scattering pattern and the associated structure factor S(q) was shown in Figure XX. The ratio of the higher-order peak position to first peak position (q/q_1) matched $1 : \sqrt{4/3} : \sqrt{8/3} : \sqrt{11/3} : 2 : \sqrt{16/3}\ldots$, confirming the formation of FCC lattice.

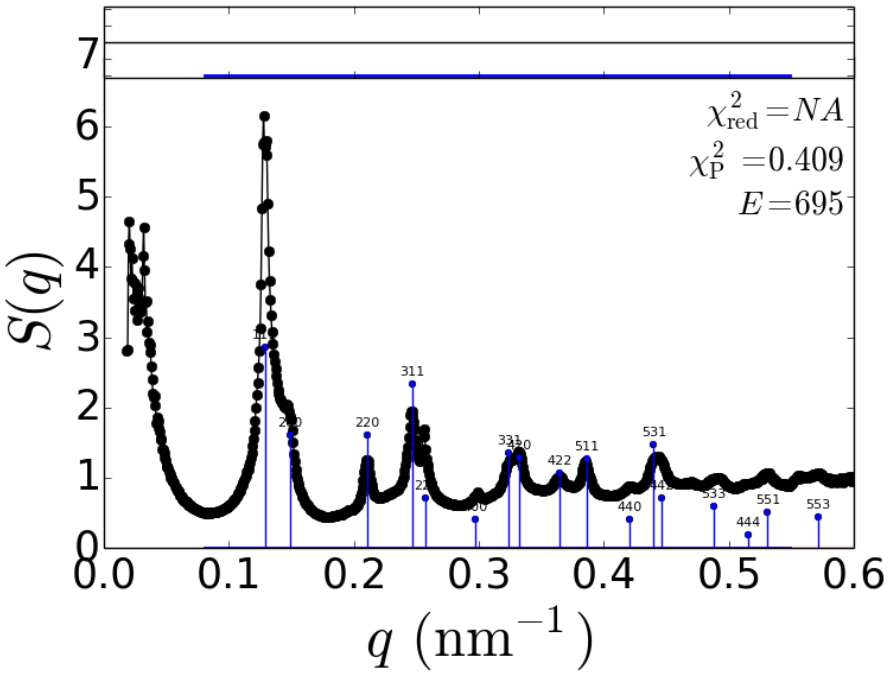

Figure S2. SAXS pattern of FCC lattice consisting of 15 nm AuNPs and DNA tetrahedral frames collected in aqueous solution. Structure factors are plotted on the linear scale, Miller indices are marked for each reflex in the range.

DNA octahedron frame could also assemble gold nanoparticles into FCC lattice. The DNA octahedron frame was composed of 12 six-helix bundle edges with a length of 28.6 nm. One single-stranded DNA was designed at both ends of each bundle for binding with a spherical gold nanoparticle. At each vertex, one gold nanoparticle with a core diameter of 10 nm was anchored by four anchoring strands. However, gold nanoparticles have two different connection manners

with DNA frames. Each nanoparticle in-plane was shared by four DNA frames to form an octahedron layer. The octahedron layers were linked by nanoparticles; each of them was shared by two DNA frames. Thus, the ratio of DNA octahedrons to gold nanoparticles is 1:2 in the FCC lattice. A series of sharp scattering peaks were shown in the 2D scattering and the associated structure factor S(q). The ratio of peak position (q/q_1) showed 1 :$\sqrt{4/3}$: $\sqrt{8/3}$: $\sqrt{11/3}$: 2: $\sqrt{16/3}$…, in a good agreement with the calculated S(q) profile for an FCC lattice.

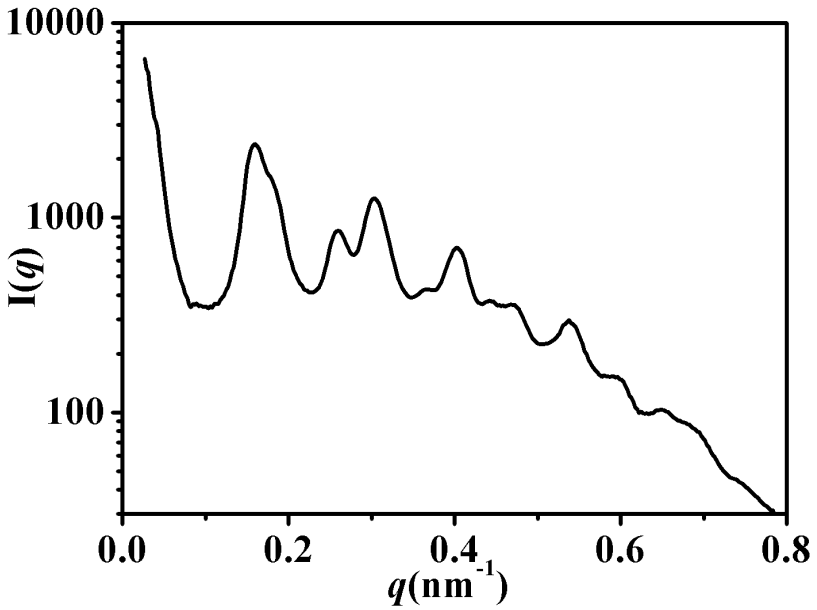

Figure S3. SAXS pattern of FCC lattice consisting of 10 nm AuNPs and DNA octahedral frames measured in aqueous solution. Intensity plotted in the logarithmic scale.

In addition to FCC lattice, SC lattice could also be assembled by DNA origami frame and gold nanoparticles. To assemble SC lattice, DNA cubes and gold nanoparticles with a core diameter of 10 nm were mixed with a ratio of 1:2. DNA cube has a similar edge length and diameter with DNA octahedron. Same as the design of anchoring strands on the DNA octahedron, each vertex of DNA cube has four anchoring strands to bind one nanoparticle and connect them into the SC lattice. The formation of SC lattice was further confirmed by SAXS measurement. The ratio of peak position (q/q_1) exhibits 1 :$\sqrt{2}$: $\sqrt{3}$: 2…, indicating the formation of the SC lattice.

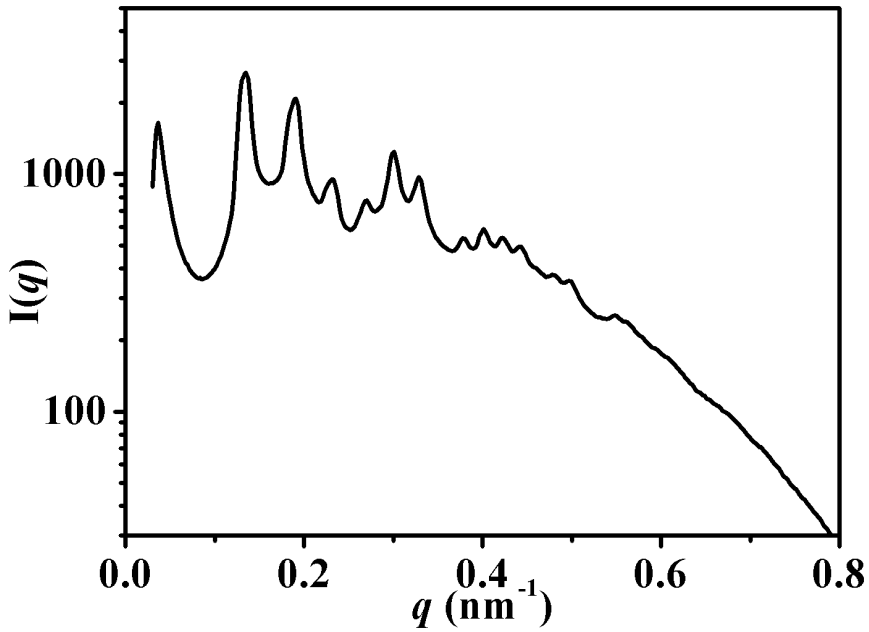

Figure S4. SAXS pattern of the SC lattice consisting of 10 nm AuNPs and DNA cubic frames measured for sample in aqueous solution.

Silica coating process

Time series

Silica-coating reaction can be carried out at 4 °C, however it takes substantially longer to complete. Below, in Figure S5 we show a series of TEM images taken of samples incubated in a coating solution with 1:20:10 and 1:20:15 DNA:Linker:TEOS molar ratio at different time intervals. The hydrolysis reaction is incomplete after 4 hours, particularly for the sample with lower concentration of TEOS.

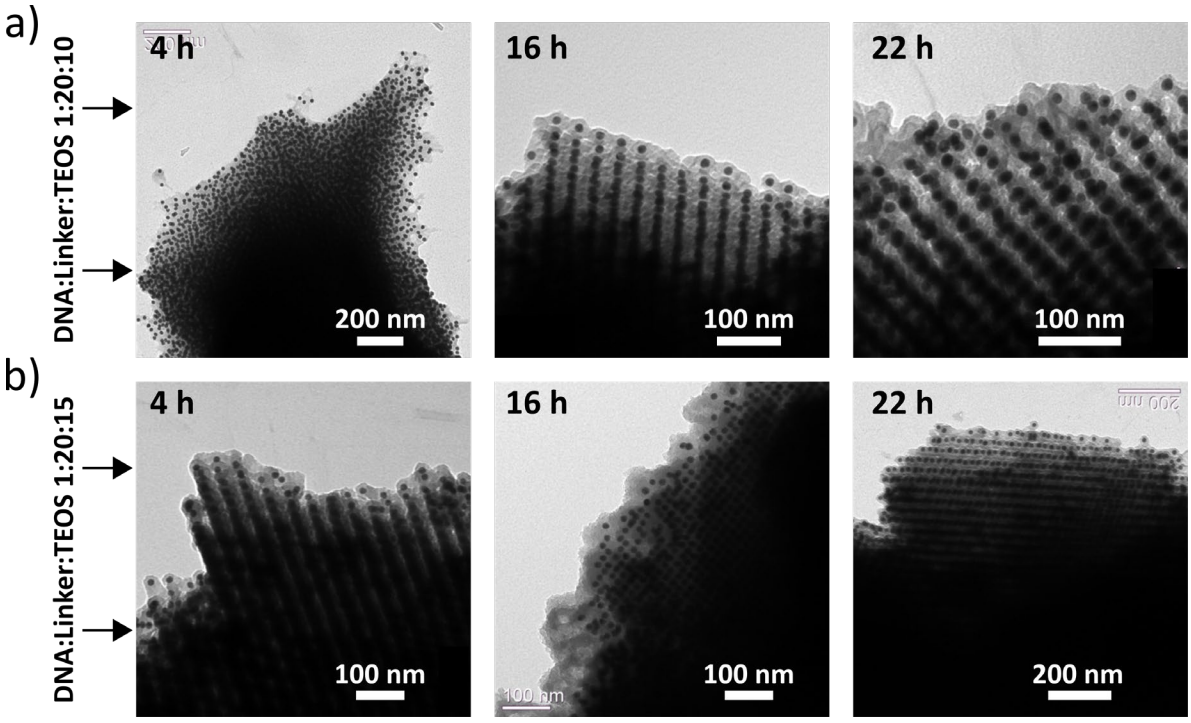

Figure S5. **Coating time influence at a constant (high) concentration of the linker.** Room temperature bright-field TEM (BF-TEM) micrographs of silica-coated FCC DNA-AuNPs superlattice composed of tetrahedral DNA origami units. **(a)** 1:20:10 DNA:Linker:TEOS coating buffer composition (**b)** 1:20:15 DNA:Linker:TEOS coating buffer composition. All samples were incubated in the coating buffer at 4 °C.

Coating thickness and mechanical stability

Thickness coating and mechanical stability of the superlattices are affected by the amount of the linker (TMAPS) and TEOS used in the coating reaction. The stability can be qualitatively assessed by TEM imaging of the samples air-dried on TEM grids; the samples which are coated too thinly collapse upon drying even when dried from low-surface tension solvents. The stability of the coated FCC lattices is influenced both by the amount of linker (without the linker, coating cannot be accomplished irrespective of the amount of TEOS used) and TEOS since both chemical species possess reactive ethoxide groups which can cross-react to form silica cladding. The concentration threshold which provides air-stable samples was observed near 1:10:20 ratio (DNA:Linker:TEOS) in the series where linker concentration was held constant at 1:10 DNA:Linker ratio (Figure S6a) and near 1:20:10 (DNA:Linker:TEOS) if higher linker concentration, 1:20 (DNA:Linker) was used (Figure S6b). The stability series is shown in Figure S6, where the ratios of DNA:Linker:TEOS are reported in the top-left corner of representative TEM images. All samples were incubated in the coating buffer for 16 h at 4 °C.

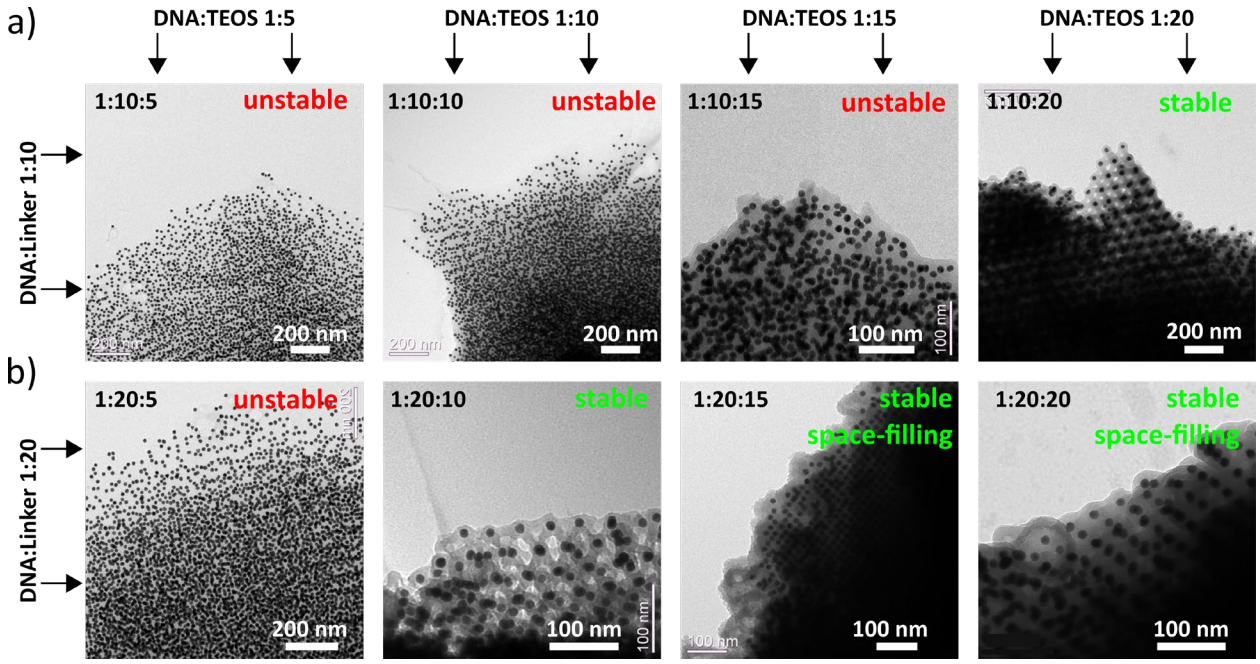

Figure S6. The influence of the linker (TMAPS) and TEOS concentration on air-stability of silica-coated FCC DNA-AuNPs superlattice composed of tetrahedral DNA origami units. BF-TEM images of samples obtained at constant DNA to linker molar ratios **a)** 1:10 (DNA:Linker) and **b)** 1:20 (DNA:Linker). Concentration of TEOS increases along the rows in the table. All samples were incubated in the coating buffer for 16 h at 4 °C.

Electron microscopy studies of DNA-gold nanoparticle superlattices.

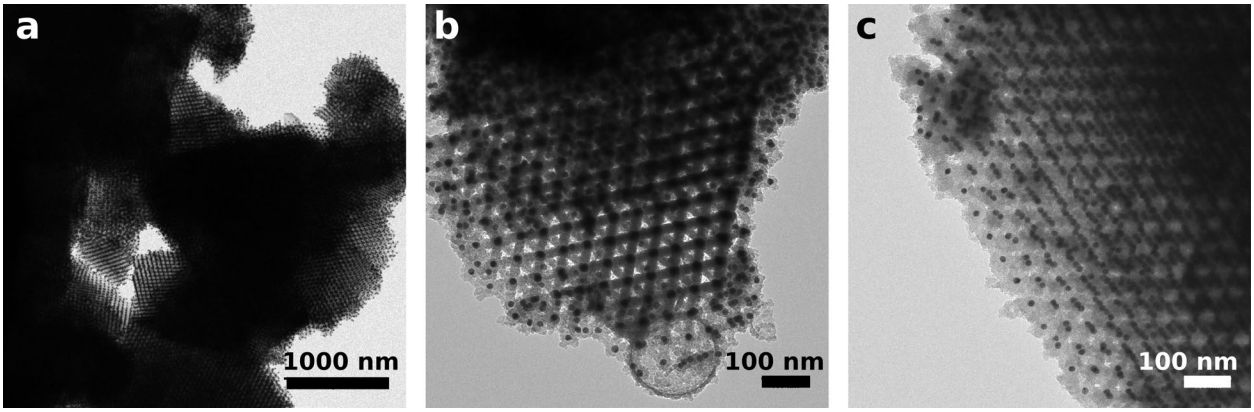

Figure S7. **Room temperature bright-field TEM (BF-TEM) micrographs of the silica-coated FCC DNA-AuNPs superlattice composed of tetrahedral DNA origami units. (a)** Low and high (**b)** magnification images of the sample where SiO_2 forms 5 nm thick layer around DNA bundles (15 nm of apparent strut's diameter), occupying approximately 20% of available volume. **(c)** Completely coated superlattice, referred to as "100% silica-coated".

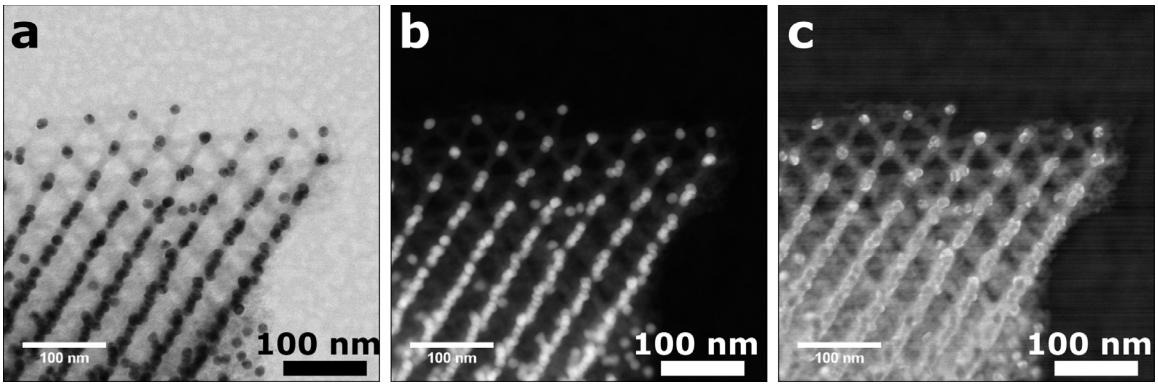

Figure S8. **Room temperature scanning TEM (STEM) micrographs of the silica-coated FCC DNA-AuNPs superlattice composed of tetrahedral DNA origami units. a)** Bright-field image (BF-STEM), **b)** high-angle annular dark-field image (HAADF-STEM), darkfield images obtained using detectors positioned at an intermediate angle — DF4 **(c)**.

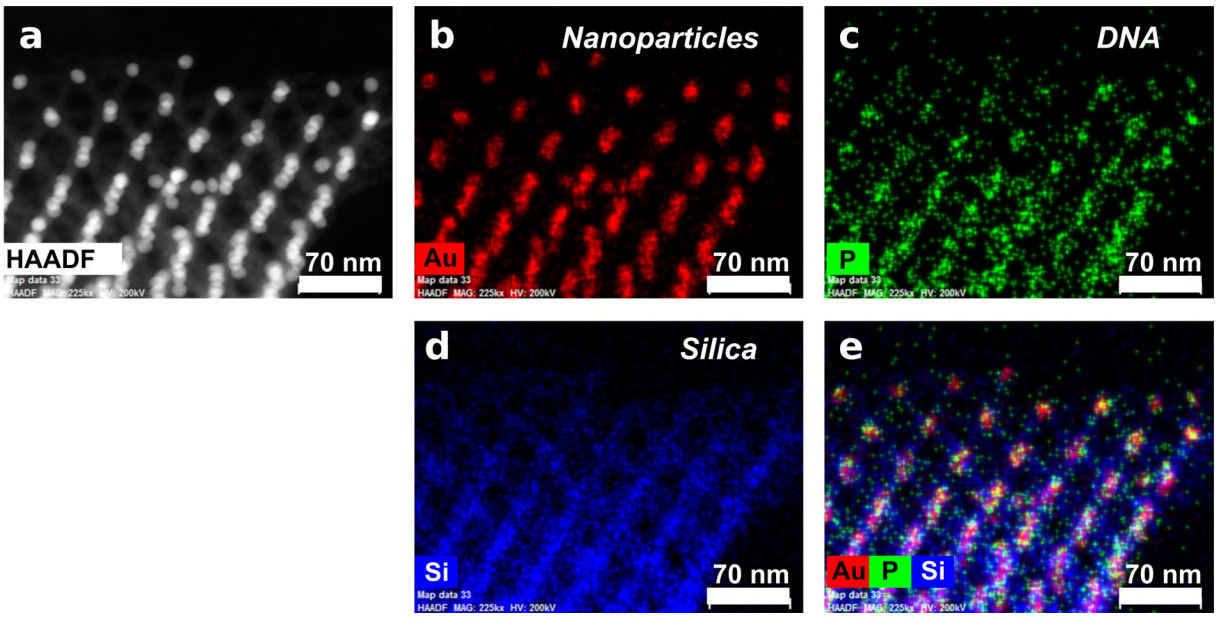

Figure S9. Room Temperature STEM EDS of silica-coated FCC DNA-AuNPs superlattice composed of tetrahedral DNA origami units. a) High angle annular dark-field scanning TEM micrographs of FCC DNA-AuNPs superlattice composed of tetrahedral building blocks after air drying. EDX elemental distribution mapping (raw x-ray counts) of gold (AuNPs) **(b)**, phosphorus (DNA strands) **(c)**, Si, (SiO_2 silica) (**d**), Au, P, Si elemental maps overlaid on HAADF image **(e)**.

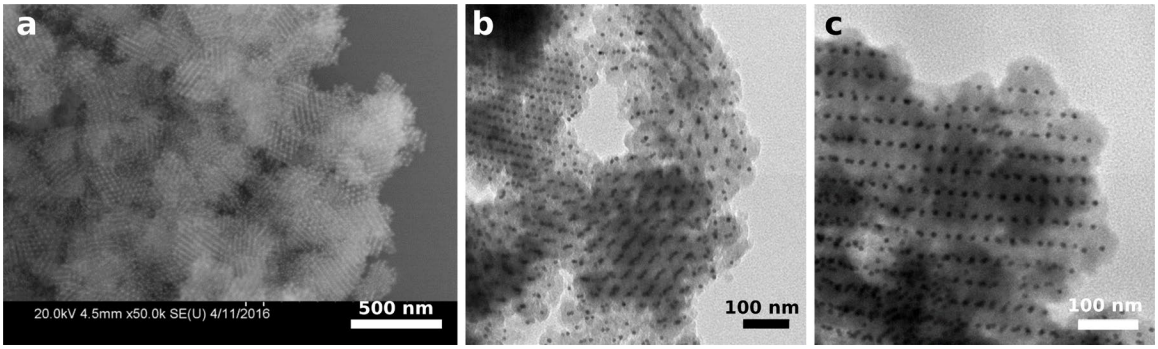

Figure S10. **Electron microscope micrographs of air-dried FCC DNA-AuNPs superlattice composed of octahedral DNA origami units coated with silica to a near-saturation extent**. **(a)** Low magnification SEM image, (**b and c)** BF-TEM images.

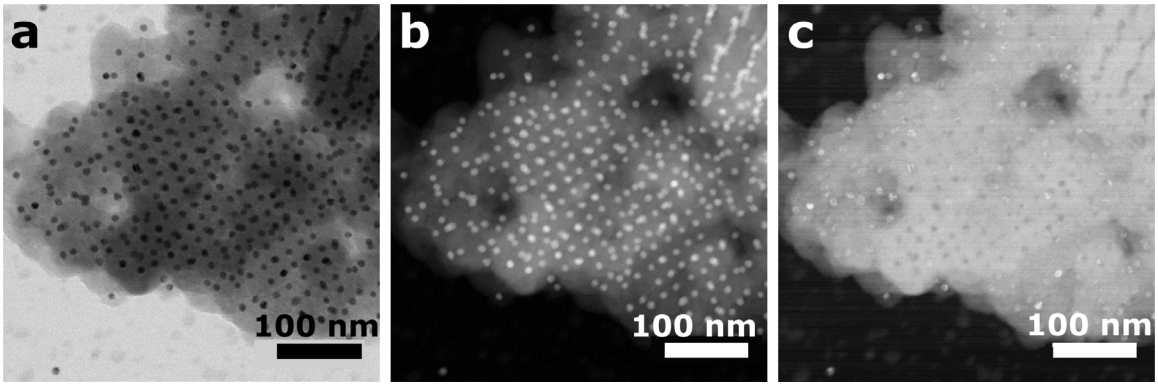

Figure S11. **Room temperature scanning TEM (STEM) micrographs of the silica-coated FCC DNA-AuNPs superlattice composed of octahedral DNA origami units coated with silica to a near-saturation extent**. **a)** Bright-field image (BF-STEM), **b)** high-angle annular dark-field image (HAADF-STEM), darkfield images obtained using detectors positioned at an intermediate angle — DF4 **(c)**.

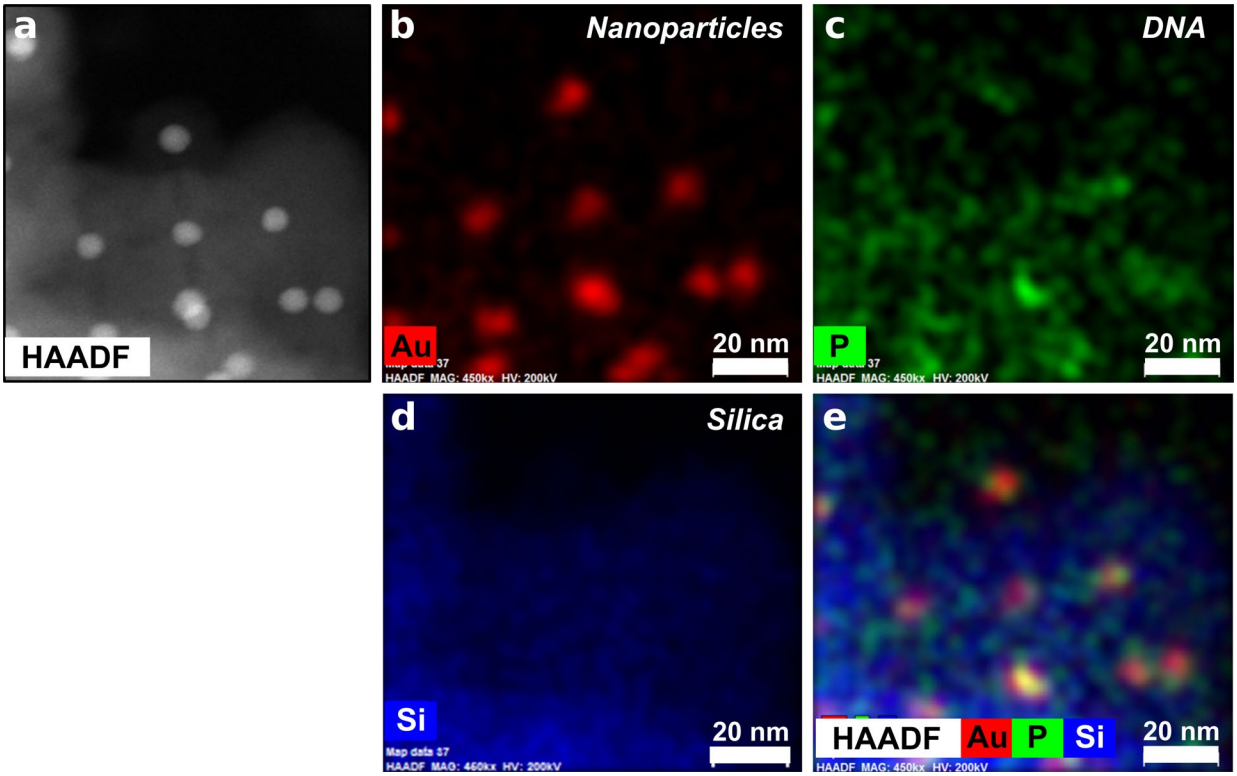

Figure S12. STEM micrographs of air-dried silica-coated superlattice composed of octahedral DNA-AuNPs origami building blocks a) High angle annular dark-field scanning TEM micrographs of an isolated octahedral structural motif with visible voids (lower electron density region) along the DNA tubules connecting gold NPs. EDX elemental mapping (raw x-ray counts) of gold (AuNPs), **(b)** phosphorus (DNA strands) **(c)** Si, (SiO_2 silica), **d**) Au, P, Si elemental maps overlaid on HAADF image **(e)**. The sample is coated with silica to a near-maximum extent.

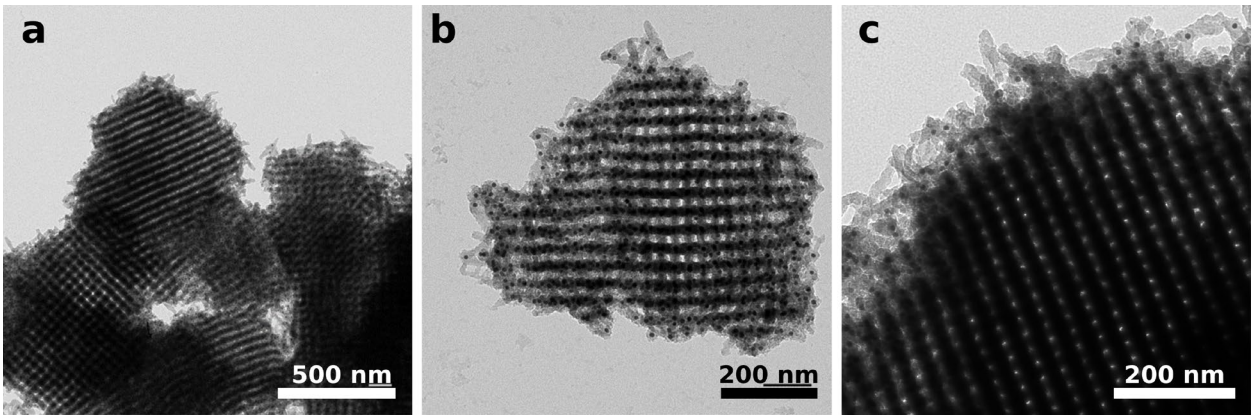

Figure S13. **Room temperature bright-field TEM (BF-TEM) micrographs of the silica-coated SC DNA-AuNPs superlattice composed of cubic DNA origami units**. Silica occupies approximately 40% of the sample volume. **(a)** Low and high **(b, c)** magnification images reveal highly-regular arrangements of open channels in each grain (monodomain).

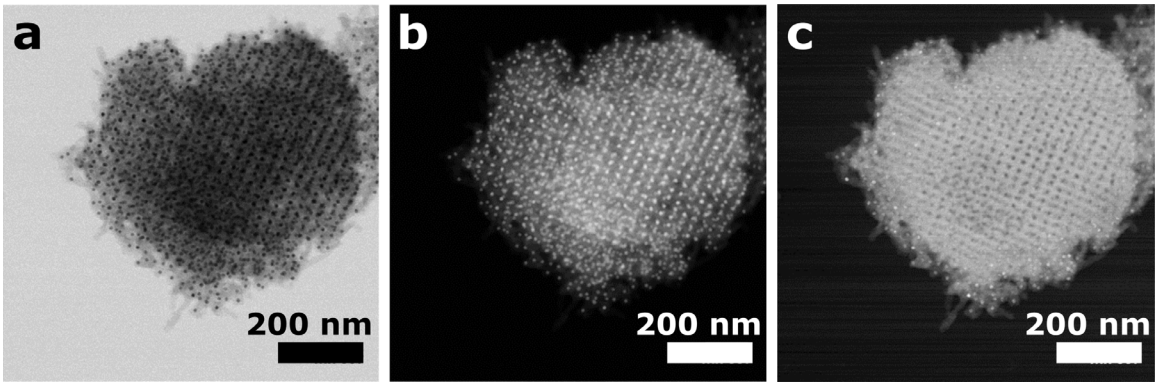

Figure S14. **Room temperature scanning TEM (STEM) micrographs of the silica-coated SC DNA-AuNPs superlattice composed of cubic DNA origami units. a)** Bright-field image (BF-STEM), **b)** high-angle annular dark-field image (HAADF-STEM), darkfield images obtained using detectors positioned at an intermediate angle — DF4 **(c)**.

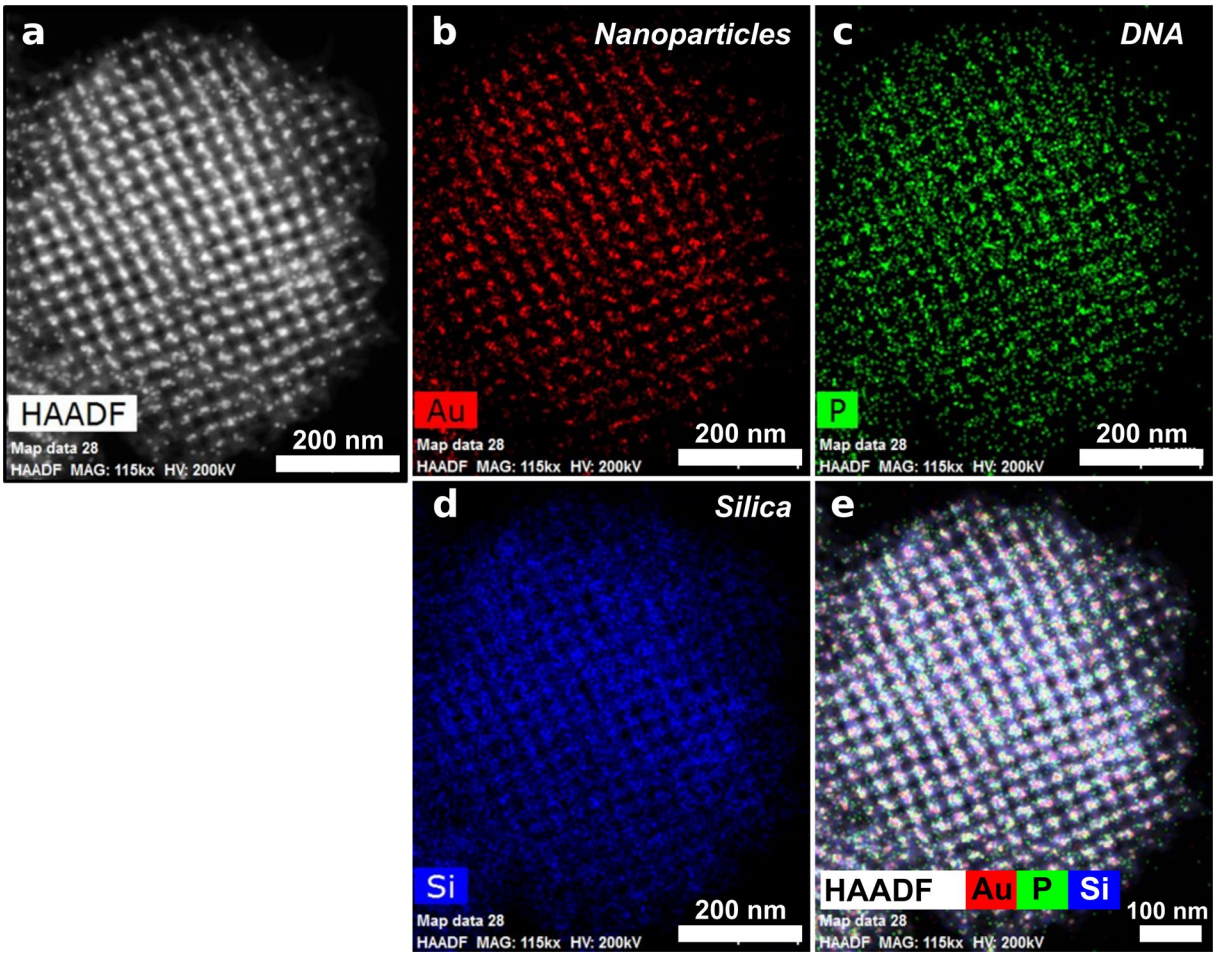

Figure S15. Scanning TEM EDX (STEM-EDS) micrographs of the silica-coated SC DNA-AuNPs superlattice composed of cubic DNA origami units.a) High angle annular dark-field scanning TEM micrographs of the SC DNA-AuNPs superlattice after air drying. EDX elemental distribution mapping (raw x-ray counts) of gold (AuNPs) **(b)**, phosphorus (DNA strands) **(c)**, Si, (SiO_2 silica) (**d**), Au, P, Si elemental maps overlaid on HAADF image **(e)**.

Thermal stability of silica scaffold.

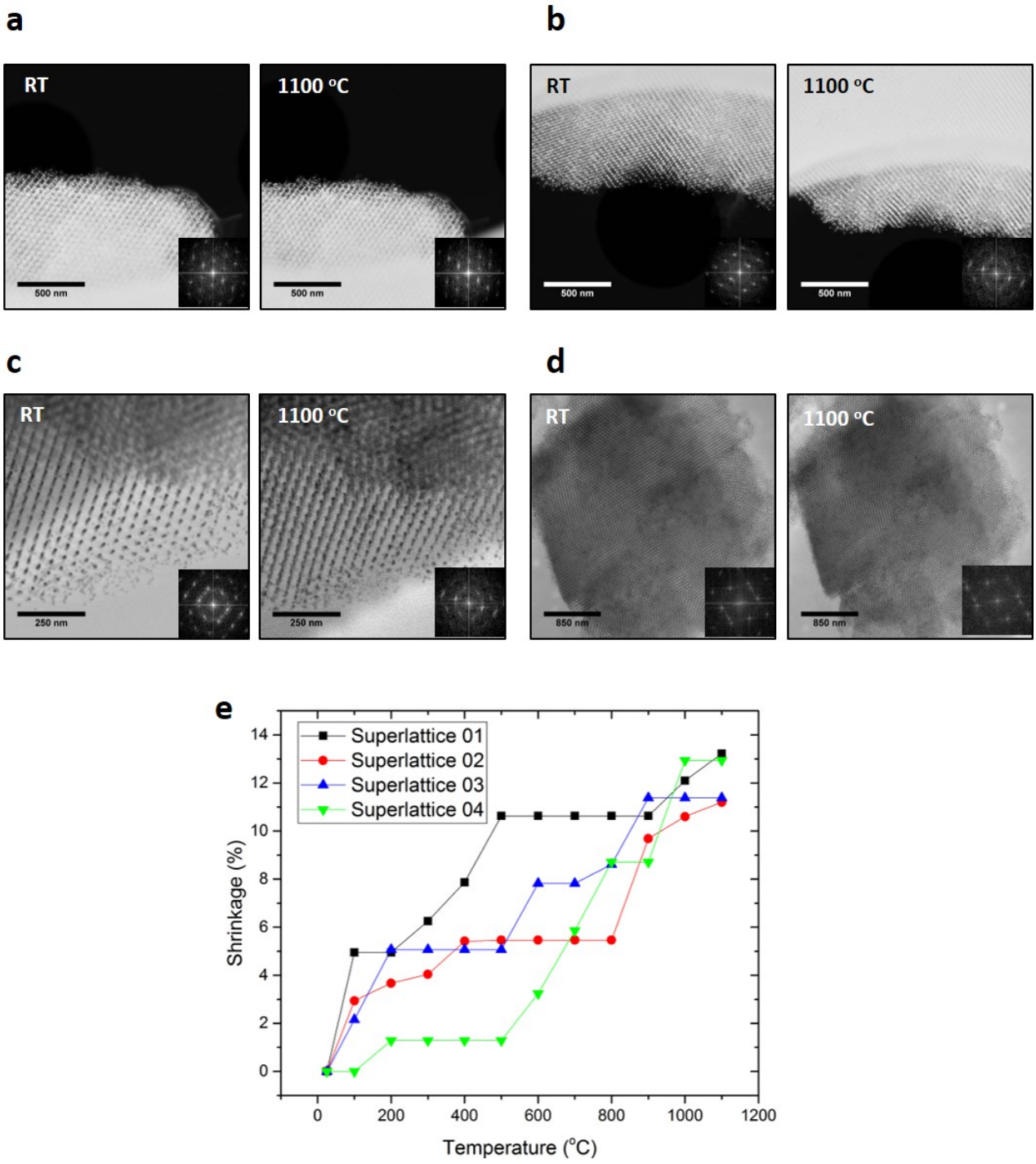

Figure S16. **Analysis of the DNA-AuNPs FCC tetrahedral superlattice shrinking process over the temperature increasing, from room temperature to 1100 °C**. **a)–b)** HAADF-STEM images and **c)–d)** BF-STEM images showing superlattice structures at room temperature and 1100 °C. The inserted FFT of each image infers no structural order changing. The superlattice retains its structure over the whole range of temperatures tested, however, the FFT shows a modest

shrinkage of the lattice constant at elevated temperatures compared with the samples air-dried at room temperature corroborating the SAXS results (Fig 4 of the main text) (**e)**).

The values of superlattice shrinkage plotted in Figure 4a in the main text and Figure S5 are reported as a fractional contraction of the unit cell constant during the heating relative to the initial, dry-state, room temperature value inferred from SAXS data or FFT of TEM images.

Elemental maps by EDS/STEM at elevated temperatures.

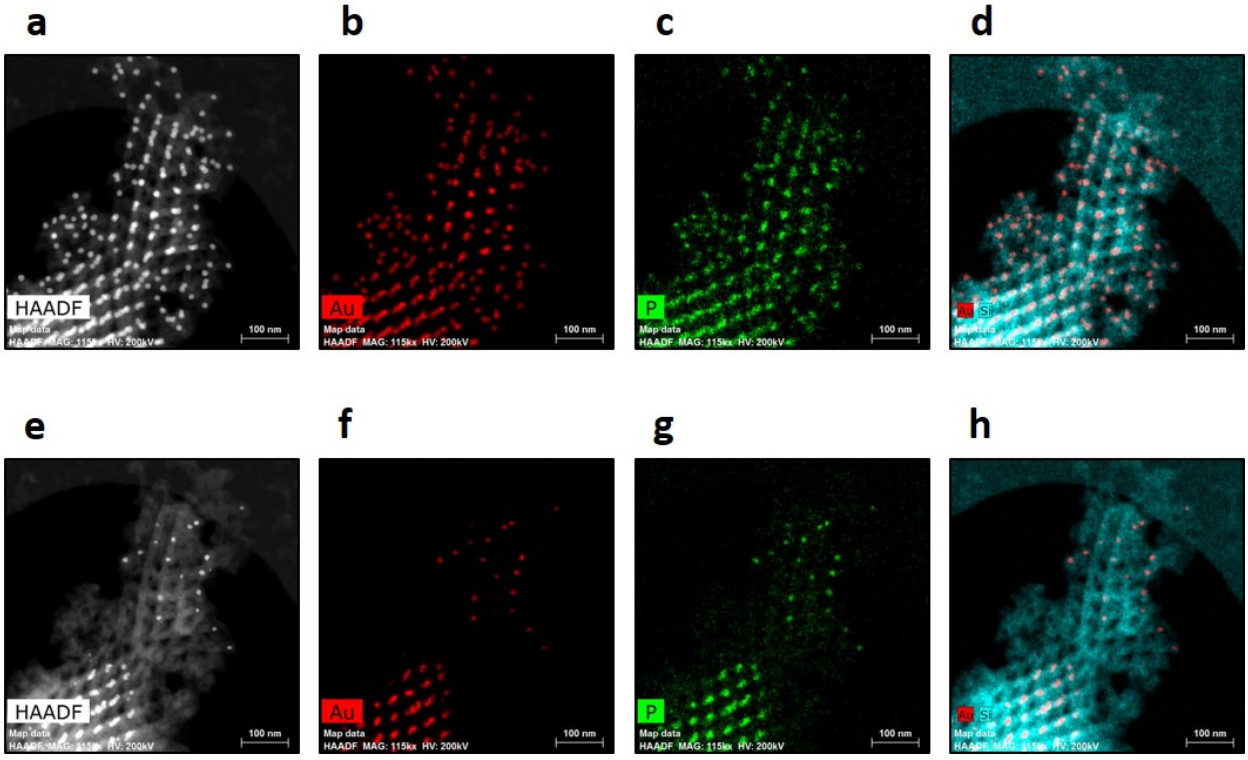

Figure S17. **EDS analysis (raw x-ray counts) of the FCC DNA-AuNPs superlattice a)–d)** before and **e)–h)** after a heating cycle. **a)**, **e)** HAADF-STEM; **b)**, **f)** Au mapping; **c)**, **g)** P mapping; **d)**, **h)** Si and Au mapping. After the heating (0.5 ºC/s) from room temperature to 1200 ºC, waiting time of 10 min, and then cooling (−0.5 °C/s) to room temperature, it is observed the AuNPs shrinking and vanishing. Because there is no trace of Au over the rest of the SiO_2 scaffold after the heating cycle (**h)**), the melting and evaporation processes have taken place as opposed to Au dispersion over the lattice by diffusion.

Dark-field STEM after isothermal heating at 1200 ºC

In this experiment, we have verified that the steady disappearance of gold nanoparticles during the in-situ thermal ramps is not caused by the electron-beam damage and is rather a result of the evaporation of material. As indicated by the STEM image in Fig. S5a which was taken only after very brief illumination with the e-beam, the evaporation is not limited to the areas that are directly exposed to the beam and can be seen in the entire sample. This process, however, might not be instantaneous nor uniform across the specimen as thermal gradients along the structures are expected. In fact, it is observed the AuNPs vanishing occurs initially outer of the DNA-AuNPs superlattices (green circles in the images), while the inner AuNPs last longer (blue circles in the images).

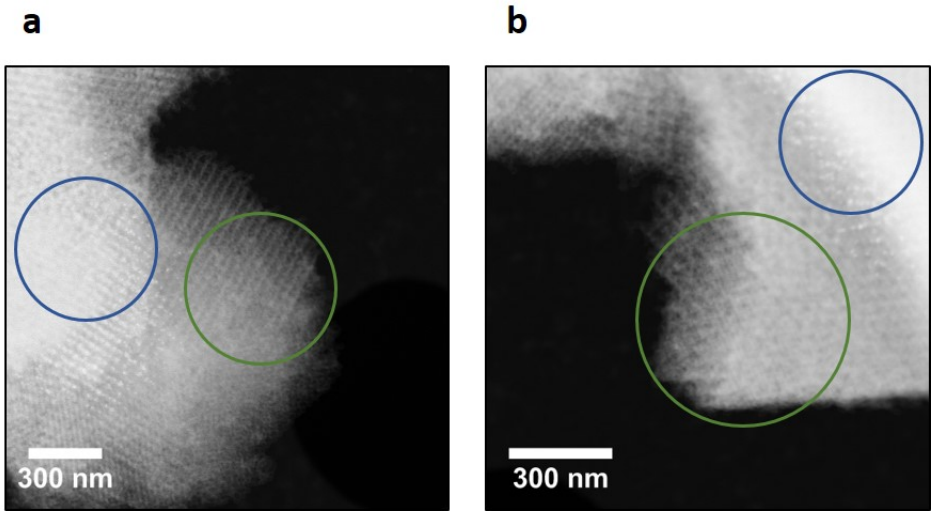

Figure S18. **Dark-field STEM of Isothermal Heating of FCC tetrahedral DNA-AuNPs Superlattices a)** and **b)** HAADF-STEM images of FCC tetrahedral DNA-AuNPs superlattices after the AuNPs vanishing process starting, at 1200 °C. During the isothermal *in-situ* heating up to 1200 °C (the upper temperature limit of our holders), these areas were not illuminated by electron beam, *i.e.*, the electron beam was away of these areas. Just after reaching 1200 °C, the sample was moved and immediately recorded the found structures. Because it is observed the same phenomena under and away of the electron beam, the process is not induced by radiation damage. Besides, because the heating transfer is mainly due to the thermal conduction and localized radiation, thermal gradients along the structures are expected. It has been observed that the AuNPs vanishing occurs initially near the outer edge of superlattices (green circles in the images), while the inner AuNPs last longer (blue circles in the images).

In-situ TEM movie description

In-situ movies of the FCC-tetrahedral silicated samples were recorded during the heating and cooling ramps under STEM observation. Movie S1 is a 12× accelerated playback of the frames of HAADF and ADF data shown in top-left and bottom-left panels, respectively, along with the corresponding 2D FFTs of the HAADF images (top-right). The temperature ramp is plotted in the bottom-left quadrant of the screen. The onset of gold evaporation is marked by the disappearance of higher-order signals in FFT above 1300 K, which to a good approximation matches the melting point of Au (1337 K). Liquid gold evaporation is expected to be very rapid due to the high-vacuum environment but the process is impeded by silica encapsulation and slow heat transport. Movie S2 contains a zoomed-in cut from the Movie 1 shows the moment of the AuNPs melting at the actual speed of recording. Characteristic flickering of molten gold AuNPs is visible in STEM-ADF images (left panel).

High-pressure compression studies

The high-pressure experiments were performed using Almax plate diamond anvil cell with bevel culet size of Boehler-Almax diamond 450 μm. The *in-situ* x-ray scattering measurements were carried out at the SAXS beamline (CMS) of NSLS II, Brookhaven National Laboratory. The wavelength of the x-ray was 0.918 Å.

Before loading the sample into the anvil cell, we centrifuged the silica-coated sample and removed the coating buffer, then re-dispersed the centrifuged sample in a mixture of methanol, ethanol and water with volume ratio of 16:3:1, that is, the coating buffer was exchanged into the pressure-transducing medium, which kept the sample in quasi-hydrostatic condition under high pressure. The compression experiments and *in-situ* SAXS measurements were performed by gradually tightening the bolts on the diamond anvil cell assembly. At each stage of pressurization, the sample was allowed to stabilize and equilibrate for several minutes before the SAXS measurements. Hydrostatic pressure was monitored during the experiment utilizing the standard fluorescence method, tracking the separation of the R_1 and R_2 ruby lines, employing ruby ball placed in the sample cell (*68*).The maximum pressure value used in the experiment was 8 GPa.

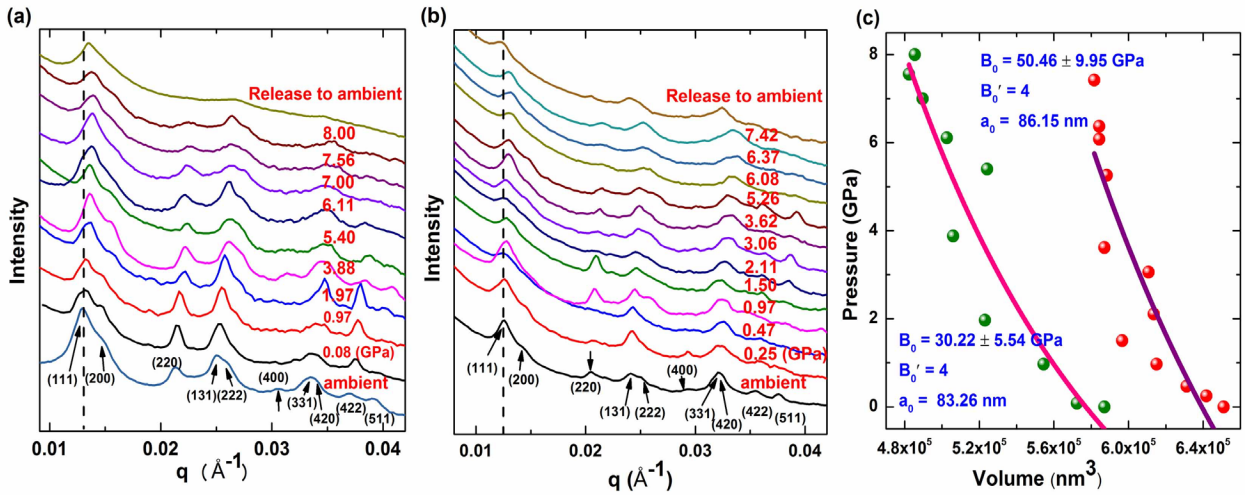

Figure S19. **Mechanical properties of the FCC SiO_2-coated superlattice under the compression stress.** Small-angle X-ray scattering (SAXS) patterns of the coated superlattice composed of DNA origami tetrahedra and 15 nm gold nanoparticles under high hydrostatic pressure generated by using Almax plate diamond anvil cell. **a**) Scattering data of the sample containing 20% silica in the interstices by volume compressed to different pressures up to 8.00 GPa. The vertical dashed line is used to guide the eye to track the 111-peak shift under increasing pressure. **b**) Scattering data of the sample fully coated with silica compressed to different pressures up to 8.00 GPa. The vertical dashed line is used to guide the eye to track the 111-peak shift under increasing pressure. **c**) The evolution of the unit-cell volume of the superlattice as a function of pressure, coated by a varied amount of SiO_2; green markers - 20% silica, red markers - 100% interstitial volume filled by silica. The solid lines indicate fitting results to the second-order Birch-Murnaghan equation of state, and the calculated bulk moduli (B_0) of the superlattice coated to a different degree with SiO_2. The error of pressure measurements is smaller than the size of the markers.

The vertical dashed lines in Figure S8 (a) and (b) are used to guide the eye clearly see the peak shift under pressure, and the Miller index of each peak is listed. From the q position of the (111) peak of the silica coated FCC superlattices, we calculated the volume of the FCC superlattice at different pressures according to the equation, $V = (\frac{2\pi\sqrt{3}}{q})^3$. Figure S8 (c) presents the volume of silica-coated FCC superlattice as a function of pressure. The green balls mark the results for the 20% silica coated FCC superlattice, the red balls —the 100% silica coated FCC superlattice. The solid lines indicate the fit of experimental data to Birch-Murnaghan equation of state (*69*), and were used to calculate the bulk moduli (B_0) of the two FCC superlattices with different thickness of silica. In the equation:

$$P(V) = \frac{3B_0}{2}[(\frac{V_0}{V})^{\frac{7}{3}} - (\frac{V_0}{V})^{\frac{5}{3}}]\{1 + \frac{3}{4}(B_0{}' - 4)[(\frac{V_0}{V})^{\frac{2}{3}} - 1]\}$$

P is hydrostatic pressure, V_0 and B_0 are the unit cell volume and bulk modulus at ambient pressure, B_0' is the first order pressure derivative of the bulk modulus.

By fixing B_0' at 4, the equation reduces to the second-order Birch-Murnaghan equation of state, which ignores the effects of pressure-dependence on B_0 allowing simpler fit and extraction of the bulk modus.

Focused Ion Beam (FIB) milling

Using the focused ion beam, slicing the sample both with or without the use of a sacrificial layer is effective to slice the sample without deformation between slices. Samples were not specifically affixed to the surface in any way other than drying. Platinum can be used to reduce charging during collection, this undesired effect can be limited by using a charge neutralizing function of the FEI Helios 660. An aggregate assembly of superlattices in silica is imaged in Figure S20 and a local region is reconstructed for visualization in Figure S21.

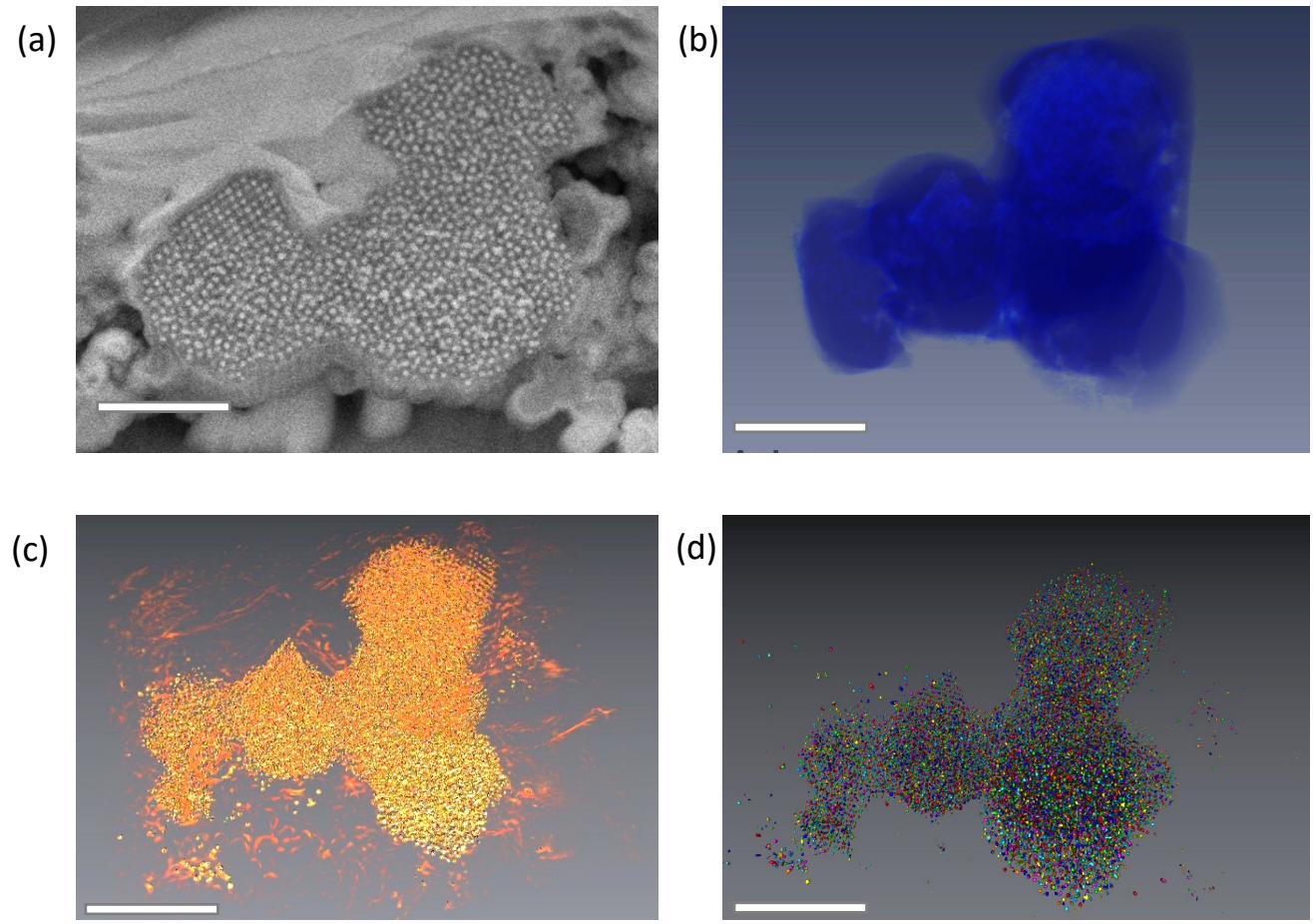

Figure S20: Serial Sectioned DNA-AuNP tetrahedral superlattices templated with Silica. (a) SEM image slice of sample region within the dataset (b) Aligned dataset, thresholding to show silica, sacrificial platinum and disordered nanoparticles. (c) Fourier filtered data retaining structures between 5 and 40nm in length (d) Segmented data using Avizo and Amira software to track individual particle positions. Scale Bar 500nm

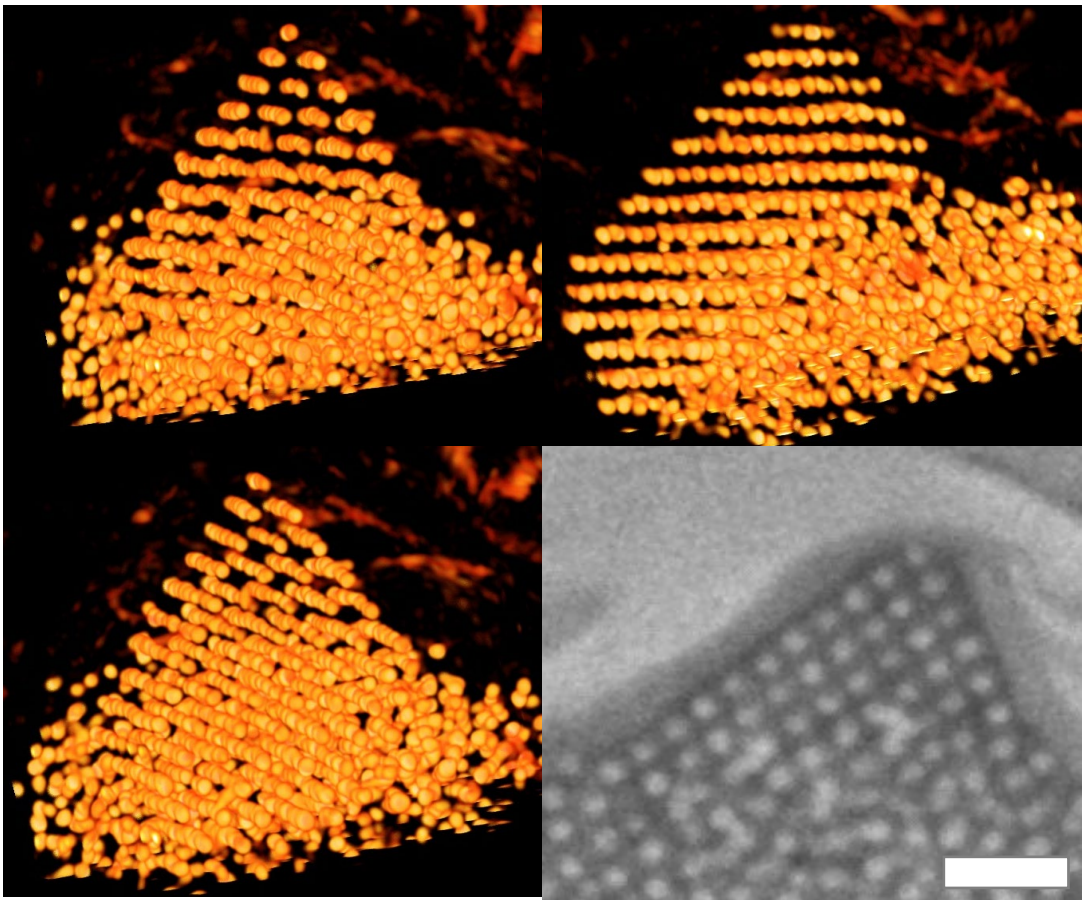

Figure S21: Multiple viewpoints of DNA-NP superlattice as 3D reconstructed from bottom-right sliced images. Scale bar 100nm. See also the supplementary videos.

Radiation exposure stability

TEM studies and synchrotron x-ray experiments demonstrated an unprecedented stability of the silica coated DNA-NP lattice to both electrons and high brilliance x-rays in comparison to the original DNA-NP lattice. Our experience with uncoated organic-inorganic DNA-AuNP lattices has shown that ~ 30 seconds of exposure to the high-photon-count sources i.e., ~1×10^{11} ph/s for CMS (11-BM) at NSLSII (BNL) is sufficient to locally degrade the sample as manifested by the reduction and eventual disappearance of scattering peaks (Figure S22). In comparison, silica-coated DNA-NP lattices were irradiated using a highly focused nanobeam (with the a size of about 10 nm) at the Hard X-ray Nanoprobe (HXN, 3-ID) at NSLSII. The silica-coated sample sustained over 5 seconds per pixel of nano-focused exposure before any sign of damage (Figure S23). At the end of the exposure, a small hole began to appear. Accounting for the area and volume, a dose of 3×10^{16} Gy (grays, J/kg) was delivered to the material.

Given the typical dose for 1×10^{7} Gy (for 30 seconds) for CMS beamline (NSLS II) (beam 200 µm × 200 µm, sample thickness <2.5mm), the silication increase a resilience to the exposed radiation of the native DNA-NP lattice by about 6 orders of magnitude (Table T1).

The dose is estimated from the exposure time (CMS: 30 seconds, HXN: 5.5 seconds), the energy of the photons (CMS: 13.5KeV and HXN: 12 KeV). The volume is calculated from the exposed area (CMS: 100um beam, HXN: <13nm beam) and sample thickness (CMS: <2.5mm, HXN 2um). The Dose/Volume is converted to grays by dividing by effective density of the silica (2700 kg/m^3) and gold (19300 kg/m^3) in the superlattice estimated as 3000 kg/m^3 (97% silica by volume, 3% AuNP), calculated similarly for the un-silicated sample as 2000 kg/m^3 using a similar estimation. This yields Gy in Joule/Kg.

Table ST1. Dosage Calculation

Beamline	HXN	CMS
X-ray Flux (photons/second)	1.00E+09	9.87E+10
Dose (total joules)	1.06E-05	6.39E-03
Volume (m^3)	2.00E-22	2.50E-13
Dose/Volume	5.28E+16	2.56E+10
Est Density	3.10E+03	2.23E+03
Grays	1.70E+13	1.15E+07

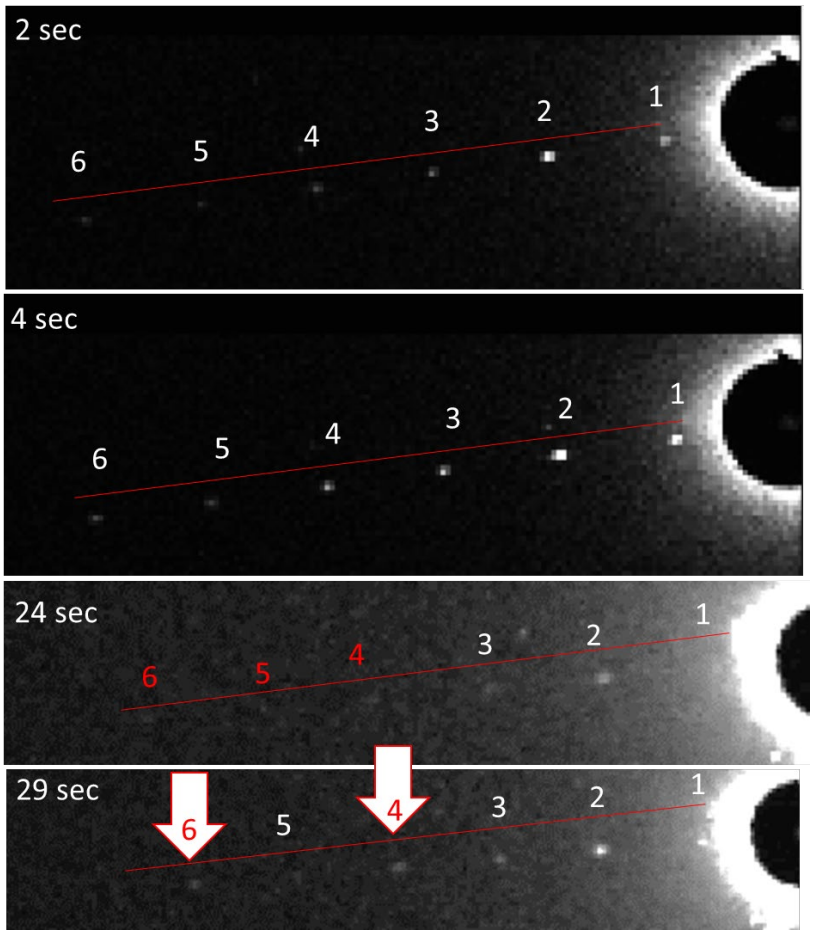

Figure S22. Beam damage to unprotected DNA superlattices at the CMS beamline (NSLSII, BNL). These subsequent exposures are contrast adjusted to make the peaks visible. After 24 and 29 seconds the sample scattering peaks start to degrade with peaks 4,5,6 either disappearing or significantly weakened compare to the shorter exposures. The first peak corresponds to 114nm, q=0.0055 $Å^{-1}$. The subsequent peaks are higher order peaks. 57, 38, 28, 23, 19nm each. Corresponding to a, a/2, a/3, a/4, a/5, a/6.

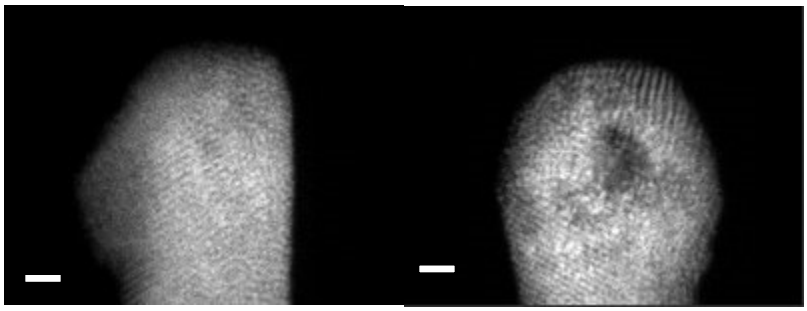

Figure S23. Beam damage to silicate coated DNA-NP lattice using x-ray microscopy with 10 nm focused beam at HXN beamline (NSLSII, BNL). The sample was imaged using x-rays, a nanobeam was rastered across the sample at a specific view angle relative to the beam direction with before: -90 degrees (left) and after: +90 degrees (right) in which a hole (black area) began to appear through the sample bulk. Scalebar: 200nm.

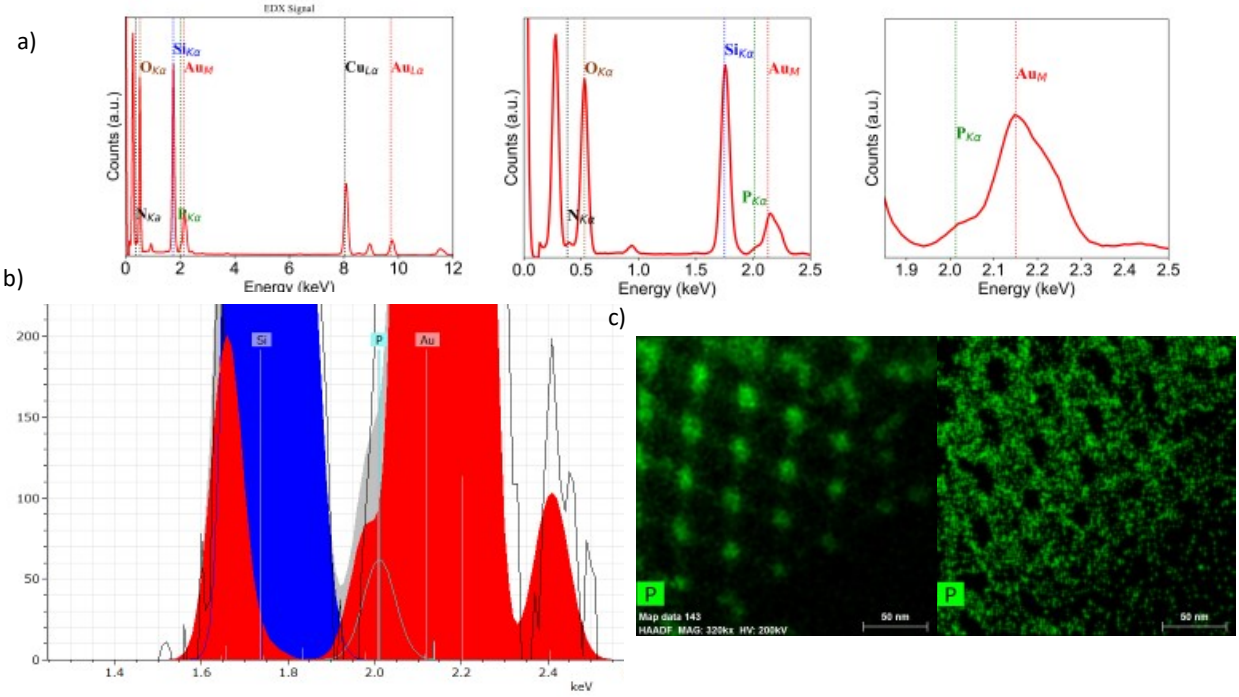

Figure S24. Summed EDS spectrum and deconvolution a) (From left to right) Summed EDS Spectrum from 0-12 KeV with peaks labeled from N, O, Si, Au-M, P, Cu, Au-L peaks. With the zoomed in region from 0-2.5 KeV reproduced from the main text along with a zoomed in region of the P and Au overlapping peaks. b) Deconvolution performed using Bruker ESPRIT software which includes detector corrections, background Bremsstrahlung, followed by Series fit deconvolution seen in figure over the Phosphorous peak location. c) Phosphorous EDS map before and after correction.

Supplemental Movie Descriptions

Movie S1 and Movie S2: In-situ Heating of FCC-tetrahedral Silica Structures in STEM

In-situ TEM movie description:

In-situ movies of the FCC-tetrahedral silicated samples were recorded during the heating and cooling ramps under STEM observation. **Movie S1** is a 12× accelerated playback of the frames of HAADF and ADF data shown in top-left and bottom-left panels, respectively, along with the corresponding 2D FFTs of the HAADF images (top-right). The temperature ramp is plotted in the bottom-left quadrant of the screen. The onset of gold evaporation is marked by the disappearance of higher-order signals in FFT above 1300 K, which to a good approximation matches the melting point of Au (1337 K). Liquid gold evaporation is expected to be very rapid due to the high-vacuum environment but the process is impeded by silica encapsulation and slow heat transport. **Movie S2** contains a zoomed-in cut from the Movie 1 shows the moment of the AuNPs melting at the actual speed of recording.

Movie S3 and S4. Serial Stack of FIB/SEM images of Silica-Superlattice with 20nm Au nanoparticles.

Processed 2D SEM images files from FIB/SEM serial sectioning. The full dataset shows a number of regions with ordered Tetrahedral-AuNP superlattice amidst disordered regions. A zoomed in subsection of the dataset, **Movie S4**, is the region selected for reconstruction and viewing in **Movie S5.**

Movie S5. 3D Reconstruction of FCC-Tetrahedral Structure

3D Reconstruction movie description:

Movie S5 file visualizing 3D Reconstruction of FCC-tetrahedral silicated sample collected from FIB-SEM. The visualized reconstruction shows the nanoparticles in the FCC structure with the silica and origami not visible. The lattice rotates about the z axis to visualize the crystal from multiple directions which reveal the structure growing from a disordered region.

These movies have been provided as separate files and are available in the online version of this document.

REFERENCES AND NOTES

1. N. C. Seeman, Nucleic acid junctions and lattices. *J. Theor. Biol.* **99**, 237–247 (1982).
2. A. P. Alivisatos, K. P. Johnsson, X. Peng, T. E. Wilson, C. J. Loweth, M. P. Bruchez Jr., P. G. Schultz, Organization of 'nanocrystal molecules' using DNA. *Nature* **382**, 609–611 (1996).
3. C. A. Mirkin, R. L. Letsinger, R. C. Mucic, J. J. Storhoff, A DNA-based method for rationally assembling nanoparticles into macroscopic materials. *Nature* **382**, 607–609 (1996).
4. E. Winfree, F. Liu, L. A. Wenzler, N. C. Seeman, Design and self-assembly of two-dimensional DNA crystals. *Nature* **394**, 539–544 (1998).
5. C. Mao, W. Sun, N. C. Seeman, Designed two-dimensional DNA holliday junction arrays visualized by atomic force microscopy. *J. Am. Chem. Soc.* **121**, 5437–5443 (1999).
6. P. W. K. Rothemund, Folding DNA to create nanoscale shapes and patterns. *Nature* **440**, 297–302 (2006).
7. M. Shekhirev, E. Sutter, P. Sutter, In situ atomic force microscopy of the reconfiguration of on-surface self-assembled DNA-nanoparticle superlattices. *Adv. Funct. Mater.* **29**, 1806924 (2019).
8. S. M. Douglas, H. Dietz, T. Liedl, B. Högberg, F. Graf, W. M. Shih, Self-assembly of DNA into nanoscale three-dimensional shapes. *Nature* **459**, 414–418 (2009).
9. N. C. Seeman, O. Gang, Three-dimensional molecular and nanoparticle crystallization by DNA nanotechnology. *MRS Bull.* **42**, 904–912 (2017).
10. J. Zheng, J. J. Birktoft, Y. Chen, T. Wang, R. Sha, P. E. Constantinou, S. L. Ginell, C. Mao, N. C. Seeman, From molecular to macroscopic via the rational design of a self-assembled 3D DNA crystal. *Nature* **461**, 74–77 (2009).
11. D. Han, S. Pal, J. Nangreave, Z. Deng, Y. Liu, H. Yan, DNA origami with complex curvatures in three-dimensional space. *Science* **332**, 342–346 (2011).
12. F. Zhang, S. Jiang, S. Wu, Y. Li, C. Mao, Y. Liu, H. Yan, Complex wireframe DNA origami nanostructures with multi-arm junction vertices. *Nat. Nanotechnol.* **10**, 779–784 (2015).
13. N. Ma, B. Minevich, J. Liu, M. Ji, Y. Tian, O. Gang, Directional assembly of nanoparticles by DNA shapes: Towards designed architectures and functionality. *Top. Curr. Chem.* **378**, 36 (2020).
14. F. Zhang, C. R. Simmons, J. Gates, Y. Liu, H. Yan, Self-assembly of a 3D DNA crystal structure with rationally designed six-fold symmetry. *Angew. Chem. Int. Ed.* **57**, 12504–12507 (2018).

15. Y. Tian, T. Wang, W. Liu, H. L. Xin, H. Li, Y. Ke, W. M. Shih, O. Gang, Prescribed nanoparticle cluster architectures and low-dimensional arrays built using octahedral DNA origami frames. *Nat. Nanotechnol.* **10**, 637–644 (2015).
16. H. Zhang, M. Li, K. Wang, Y. Tian, J.-S. Chen, K. T. Fountaine, D. DiMarzio, M. Liu, M. Cotlet, O. Gang, Polarized single-particle quantum dot emitters through programmable cluster assembly. *ACS Nano* **14**, 1369–1378 (2020).
17. E. Sutter, B. Zhang, S. Sutter, P. Sutter, In situ electron microscopy of the self-assembly of single-stranded DNA-functionalized Au nanoparticles in aqueous solution. *Nanoscale* **11**, 34–44 (2019).
18. D. Nykypanchuk, M. M. Maye, D. van der Lelie, O. Gang, DNA-guided crystallization of colloidal nanoparticles. *Nature* **451**, 549–552 (2008).
19. S. Y. Park, A. K. R. Lytton-Jean, B. Lee, S. Weigand, G. C. Schatz, C. A. Mirkin, DNA-programmable nanoparticle crystallization. *Nature* **451**, 553–556 (2008).
20. H. Xiong, D. van der Lelie, O. Gang, Phase behavior of nanoparticles assembled by DNA linkers. *Phys. Rev. Lett.* **102**, 015504 (2009).
21. D. J. Lewis, L. Z. Zornberg, D. J. D. Carter, R. J. Macfarlane, Single-crystal Winterbottom constructions of nanoparticle superlattices. *Nat. Mater.* **19**, 719–724 (2020).
22. M. Kadic, G. W. Milton, M. van Hecke, M. Wegener, 3D metamaterials. *Nat. Rev. Phys.* **1**, 198–210 (2019).
23. K. Roy, A. Jaiswal, P. Panda, Towards spike-based machine intelligence with neuromorphic computing. *Nature* **575**, 607–617 (2019).
24. J. A. Liddle, G. M. Gallatin, Nanomanufacturing: A perspective. *ACS Nano* **10**, 2995–3014 (2016).
25. M. Kjaergaard, M. E. Schwartz, J. Braumüller, P. Krantz, J. I.-J. Wang, S. Gustavsson, W. D. Oliver, Superconducting qubits: Current state of play. *Annu. Rev. Condens. Matter Phys.* **11**, 369–395 (2020).
26. W. Liu, M. Tagawa, H. L. Xin, T. Wang, H. Emamy, H. Li, K. G. Yager, F. W. Starr, A. V. Tkachenko, O. Gang, Diamond family of nanoparticle superlattices. *Science* **351**, 582–586 (2016).
27. Y. Tian, Y. Zhang, T. Wang, H. L. Xin, H. Li, O. Gang, Lattice engineering through nanoparticle–DNA frameworks. *Nat. Mater.* **15**, 654–661 (2016).
28. Y. Tian, J. R. Lhermitte, L. Bai, T. Vo, H. L. Xin, H. Li, R. Li, M. Fukuto, K. G. Yager, J. S. Kahn, Y. Xiong, B. Minevich, S. K. Kumar, O. Gang, Ordered three-dimensional nanomaterials using DNA-prescribed and valence-controlled material voxels. *Nat. Mater.* **19**, 789–796 (2020).

29. T. Zhang, C. Hartl, K. Frank, A. Heuer-Jungemann, S. Fischer, P. C. Nickels, B. Nickel, T. Liedl, 3D DNA origami crystals. *Adv. Mater.* **30**, 1800273 (2018).
30. M. R. Jones, R. J. Macfarlane, B. Lee, J. Zhang, K. L. Young, A. J. Senesi, C. A. Mirkin, DNA-nanoparticle superlattices formed from anisotropic building blocks. *Nat. Mater.* **9**, 913–917 (2010).
31. F. Lu, T. Vo, Y. Zhang, A. Frenkel, K. G. Yager, S. Kumar, O. Gang, Unusual packing of soft-shelled nanocubes. *Sci. Adv.* **5**, eaaw2399 (2019).
32. Y. Zhang, F. Lu, K. G. Yager, D. van der Lelie, O. Gang, A general strategy for the DNA-mediated self-assembly of functional nanoparticles into heterogeneous systems. *Nat. Nanotechnol.* **8**, 865–872 (2013).
33. O. Gang, A. V. Tkachenko, DNA-programmable particle superlattices: Assembly, phases, and dynamic control. *MRS Bull.* **41**, 381–387 (2016).
34. C. Tian, M. A. L. Cordeiro, J. Lhermitte, H. L. Xin, L. Shani, M. Liu, C. Ma, Y. Yeshurun, D. DiMarzio, O. Gang, Supra-nanoparticle functional assemblies through programmable stacking. *ACS Nano* **11**, 7036–7048 (2017).
35. C. Zhang, R. J. Macfarlane, K. L. Young, C. H. J. Choi, L. Hao, E. Auyeung, G. Liu, X. Zhou, C. A. Mirkin, A general approach to DNA-programmable atom equivalents. *Nat. Mater.* **12**, 741–746 (2013).
36. N. P. Agarwal, M. Matthies, F. N. Gür, K. Osada, T. L. Schmidt, Block copolymer micellization as a protection strategy for DNA origami. *Angew. Chem. Int. Ed.* **56**, 5460–5464 (2017).
37. N. Ponnuswamy, M. M. C. Bastings, B. Nathwani, J. H. Ryu, L. Y. T. Chou, M. Vinther, W. A. Li, F. M. Anastassacos, D. J. Mooney, W. M. Shih, Oligolysine-based coating protects DNA nanostructures from low-salt denaturation and nuclease degradation. *Nat. Commun.* **8**, 15654 (2017).
38. F. Bai, K. Bian, B. Li, H. Wu, L. J. Alarid, H. C. Schunk, P. G. Clem, H. Fan, Nanomaterials under stress: A new opportunity for nanomaterials synthesis and engineering. *MRS Bull.* **40**, 961–970 (2015).
39. F. Bai, K. Bian, X. Huang, Z. Wang, H. Fan, Pressure induced nanoparticle phase behavior, property, and applications. *Chem. Rev.* **119**, 7673–7717 (2019).
40. T. K. Patra, H. Chan, P. Podsiadlo, E. V. Shevchenko, S. K. R. S. Sankaranarayanan, B. Narayanan, Ligand dynamics control structure, elasticity, and high-pressure behavior of nanoparticle superlattices. *Nanoscale* **11**, 10655–10666 (2019).

41. X. Zhang, K. Hattar, Y. Chen, L. Shao, J. Li, C. Sun, K. Yu, N. Li, M. L. Taheri, H. Wang, J. Wang, M. Nastasi, Radiation damage in nanostructured materials. *Prog. Mater. Sci.* **96**, 217–321 (2018).
42. E. M. Bringa, J. D. Monk, A. Caro, A. Misra, L. Zepeda-Ruiz, M. Duchaineau, F. Abraham, M. Nastasi, S. T. Picraux, Y. Q. Wang, D. Farkas, Are nanoporous materials radiation resistant? *Nano Lett.* **12**, 3351–3355 (2012).
43. K. Keren, M. Krueger, R. Gilad, G. Ben-Yoseph, U. Sivan, E. Braun, Sequence-specific molecular lithography on single DNA molecules. *Science* **297**, 72–75 (2002).
44. J. Liu, Y. Geng, E. Pound, S. Gyawali, J. R. Ashton, J. Hickey, A. T. Woolley, J. N. Harb, Metallization of branched DNA origami for nanoelectronic circuit fabrication. *ACS Nano* **5**, 2240–2247 (2011).
45. S. Pal, Y. Zhang, S. K. Kumar, O. Gang, Dynamic tuning of DNA-nanoparticle superlattices by molecular intercalation of double helix. *J. Am. Chem. Soc.* **137**, 4030–4033 (2015).
46. N. K. Raman, M. T. Anderson, C. J. Brinker, Template-based approaches to the preparation of amorphous, nanoporous silicas. *Chem. Mater.* **8**, 1682–1701 (1996).
47. B. Kaehr, J. L. Townson, R. M. Kalinich, Y. H. Awad, B. S. Swartzentruber, D. R. Dunphy, C. J. Brinker, Cellular complexity captured in durable silica biocomposites. *Proc. Natl. Acad. Sci. U.S.A.* **109**, 17336–17341 (2012).
48. C. J. Brinker, Hydrolysis and condensation of silicates: Effects on structure. *J. Non-Cryst. Solids* **100**, 31–50 (1988).
49. C. T. Kresge, M. E. Leonowicz, W. J. Roth, J. C. Vartuli, J. S. Beck, Ordered mesoporous molecular sieves synthesized by a liquid-crystal template mechanism. *Nature* **359**, 710–712 (1992).
50. P. C. A. Alberius, K. L. Frindell, R. C. Hayward, E. J. Kramer, G. D. Stucky, B. F. Chmelka, General predictive syntheses of cubic, hexagonal, and lamellar silica and titania mesostructured thin films. *Chem. Mater.* **14**, 3284–3294 (2002).
51. R. B. Bhatia, C. J. Brinker, A. K. Gupta, A. K. Singh, Aqueous sol−gel process for protein encapsulation. *Chem. Mater.* **12**, 2434–2441 (2000).
52. J. Lee, J. Choi, J. H. Park, M.-H. Kim, D. Hong, H. Cho, S. H. Yang, I. S. Choi, Cytoprotective silica coating of individual mammalian cells through bioinspired silicification. *Angew. Chem. Int. Ed.* **53**, 8056–8059 (2014).

53. A. Désert, C. Hubert, Z. Fu, L. Moulet, J. Majimel, P. Barboteau, A. Thill, M. Lansalot, E. Bourgeat-Lami, E. Duguet, S. Ravaine, Synthesis and site-specific functionalization of tetravalent, hexavalent, and dodecavalent silica particles. *Angew. Chem. Int. Ed.* **52**, 11068–11072 (2013).
54. H. Fan, K. Yang, D. M. Boye, T. Sigmon, K. J. Malloy, H. Xu, G. P. López, C. J. Brinker, Self-assembly of ordered, robust, three-dimensional gold nanocrystal/silica arrays. *Science* **304**, 567–571 (2004).
55. E. Auyeung, R. J. Macfarlane, C. H. J. Choi, J. I. Cutler, C. A. Mirkin, Transitioning DNA-engineered nanoparticle superlattices from solution to the solid state. *Adv. Mater.* **24**, 5181–5186 (2012).
56. K. Ma, Y. Gong, T. Aubert, M. Z. Turker, T. Kao, P. C. Doerschuk, U. Wiesner, Self-assembly of highly symmetrical, ultrasmall inorganic cages directed by surfactant micelles. *Nature* **558**, 577–580 (2018).
57. T. Aubert, K. Ma, K. W. Tan, U. Wiesner, Two-dimensional superstructures of silica cages. *Adv. Mater.* **32**, e1908362 (2020).
58. M. Numata, K. Sugiyasu, T. Hasegawa, S. Shinkai, Sol–gel reaction using DNA as a template: An attempt toward transcription of DNA into inorganic materials. *Angew. Chem. Int. Ed.* **43**, 3279–3283 (2004).
59. S. Satoh, B. Fugetsu, M. Nomizu, N. Nishi, Functional DNA–silica composite prepared by sol–gel method. *Polym. J.* **37**, 94–101 (2005).
60. X. Liu, F. Zhang, X. Jing, M. Pan, P. Liu, W. Li, B. Zhu, J. Li, H. Chen, L. Wang, J. Lin, Y. Liu, D. Zhao, H. Yan, C. Fan, Complex silica composite nanomaterials templated with DNA origami. *Nature* **559**, 593–598 (2018).
61. L. Nguyen, M. Döblinger, T. Liedl, A. Heuer-Jungemann, DNA-origami-templated silica growth by sol–gel chemistry. *Angew. Chem. Int. Ed.* **58**, 912–916 (2019).
62. L. Huang, J. Kieffer, Amorphous-amorphous transitions in silica glass. I. Reversible transitions and thermomechanical anomalies. *Phys. Rev. B* **69**, 224203 (2004).
63. S. Srivastava, D. Nykypanchuk, M. M. Maye, A. V. Tkachenko, O. Gang, Super-compressible DNA nanoparticle lattices. *Soft Matter* **9**, 10452–10457 (2013).
64. J. Biener, A. M. Hodge, J. R. Hayes, C. A. Volkert, L. A. Zepeda-Ruiz, A. V. Hamza, F. F. Abraham, Size effects on the mechanical behavior of nanoporous Au. *Nano Lett.* **6**, 2379–2382 (2006).

65. S. Nambiar, J. T. W. Yeow, Polymer-composite materials for radiation protection. *ACS Appl. Mater. Interfaces* **4**, 5717–5726 (2012).
66. I. J. Beyerlein, A. Caro, M. J. Demkowicz, N. A. Mara, A. Misra, B. P. Uberuaga, Radiation damage tolerant nanomaterials. *Mater. Today* **16**, 443–449 (2013).
67. N. C. Seeman, De novo design of sequences for nucleic acid structural engineering. *J. Biomol. Struct. Dyn.* **8**, 573–581 (1990).
68. H. K. Mao, J. Xu, P. M. Bell, Calibration of the ruby pressure gauge to 800 kbar under quasi-hydrostatic conditions. *J. Geophys. Res. Solid Earth* **91**, 4673–4676 (1986).
69. P. Podsiadlo, B. Lee, V. B. Prakapenka, G. V. Krylova, R. D. Schaller, A. Demortière, E. V. Shevchenko, High-pressure structural stability and elasticity of supercrystals self-assembled from nanocrystals. *Nano Lett.* **11**, 579–588 (2011).